



# Hard X-Ray Polarization Catalog for a Five-year Sample of Gamma-Ray Bursts Using AstroSat CZT Imager

Tanmoy Chattopadhyay<sup>1</sup> , Soumya Gupta<sup>2,3</sup> , Shabnam Iyyani<sup>2,4</sup> , Divita Saraogi<sup>5</sup> , Vidushi Sharma<sup>2,6</sup> , Anastasia Tsvetkova<sup>7</sup> , Ajay Ratheesh<sup>8</sup> , Rahul Gupta<sup>9,10</sup> , N. P. S. Mithun<sup>11</sup> , C. S. Vaishnava<sup>11</sup> , Vipul Prasad<sup>2</sup> , E. Aarthy<sup>11</sup> , Abhay Kumar<sup>11</sup> , A. R. Rao<sup>2</sup> , Santosh Vadawale<sup>11</sup> , Varun Bhalariao<sup>5</sup> , Dipankar Bhattacharya<sup>2</sup> , Ajay Vibhute<sup>2</sup> , and

Dmitry Frederiks<sup>7</sup>

<sup>1</sup> Kavli Institute of Particle Astrophysics and Cosmology, Stanford University, 452 Lomita Mall, Stanford, CA 94305, USA; [tanmoyc@stanford.edu](mailto:tanmoyc@stanford.edu)

<sup>2</sup> Inter-University Center for Astronomy and Astrophysics, Pune, Maharashtra-411007, India

<sup>3</sup> Homi Bhabha National Institute, Anushakti Nagar, Mumbai Maharashtra-400094, India

<sup>4</sup> Indian Institute of Science Education and Research, Thiruvananthapuram, 695551, Kerala, India

<sup>5</sup> Department of Physics, Indian Institute of Technology Bombay, Powai, Mumbai-400076, India

<sup>6</sup> Department of Physics, KTH Royal Institute of Technology, AlbaNova, SE-10691 Stockholm, Sweden

<sup>7</sup> Ioffe Institute, Politekhnicheskaya 26, St. Petersburg 194021, Russia

<sup>8</sup> INAF—IAPS, Via Fosso del Cavaliere 100, I-00133 Rome, Italy

<sup>9</sup> Department of Physics, Deen Dayal Upadhyaya Gorakhpur University, Gorakhpur-273009, India

<sup>10</sup> Aryabhata Research Institute of Observational Sciences (ARIES), Manora Peak, Nainital-263002, India

<sup>11</sup> Physical Research Laboratory, Navrangpura, Ahmedabad, Gujarat-380009, India

Received 2022 March 14; revised 2022 July 5; accepted 2022 July 19; published 2022 August 25

## Abstract

The Cadmium Zinc Telluride Imager (CZTI) on board AstroSat has been regularly detecting gamma-ray bursts (GRBs) since its launch in 2015. Its sensitivity to polarization measurements at energies above 100 keV allows CZTI to attempt spectropolarimetric studies of GRBs. Here, we present the first catalog of GRB polarization measurements made by CZTI during its first five years of operation. This includes the time-integrated polarization measurements of the prompt emission of 20 GRBs in the energy range 100–600 keV. The sample includes the bright GRBs that were detected within an angle range of  $0^{\circ}$ – $60^{\circ}$  and  $120^{\circ}$ – $180^{\circ}$  where the instrument has useful polarization sensitivity and is less prone to systematics. We implement a few new modifications in the analysis to enhance the polarimetric sensitivity of the instrument. The majority of the GRBs in the sample are found to possess less/null polarization across the total bursts' duration in contrast to a small fraction of five GRBs that exhibit high polarization. The low polarization across the bursts might be due either to the burst being intrinsically weakly polarized or to a varying polarization angle within the burst even when it is highly polarized. In comparison to POLAR measurements, CZTI has detected a larger number of cases with high polarization. This may be a consequence of the higher energy window of CZTI observations, which results in the sampling of a shorter duration of burst emissions than POLAR, thereby probing emissions with less temporal variation in polarization properties.

*Unified Astronomy Thesaurus concepts:* [Gamma-ray bursts \(629\)](#); [Polarimetry \(1278\)](#); [X-ray astronomy \(1810\)](#); [Astronomical instrumentation \(799\)](#); [Spectropolarimetry \(1973\)](#)

*Supporting material:* figure set

## 1. Introduction

Gamma-ray bursts (GRBs; Klebesadel et al. 1973) are the sources of the brightest electromagnetic radiation known to occur in the universe. These energetic events are believed to be powered by a newly born black hole (Woosley 1993; Narayan et al. 2001) or a magnetar (Duncan & Thompson 1992; Usov 1992), formed during the core-collapse of a massive star (Woosley 1993; Iwamoto et al. 1998; MacFadyen & Woosley 1999) or the merger of compact objects (Eichler et al. 1989; Narayan et al. 1992) such as binary neutron stars (Abbott et al. 2017) or a black hole and a neutron star. The initial intense flashes of  $\gamma$ -rays occurring close to the burst site are known as prompt emission. The delayed emission, which is observed across the entire energy spectrum, is known as

afterglow (Rees & Meszaros 1992; Piran 2004; Mészáros 2006).

The unique and non-recurring transient nature of the GRB emission makes the task of developing a generic understanding of the GRB radiation mechanism highly challenging. Even after more than half a century since its discovery, the mechanism giving rise to the observed prompt emission still largely remains a key open question (Kumar & Zhang 2015; Zhang et al. 2019). Generally, the spectrum of the prompt emission is studied via fitting with various phenomenological model functions such as a power law, Band function, power law with exponential cutoff, etc. (Band et al. 1993; Gruber et al. 2014). The most popular competing radiation models are based on the jet photosphere (Rees & Meszaros 1992; Ryde 2004) and optically thin synchrotron emission (Rees & Meszaros 1994; Sari et al. 1998). Several attempts have been made to test these various physical models directly with data (Burgess 2014; Ahlgren et al. 2015, 2019; Burgess et al. 2020). However, most spectral analyses yield similar fit statistics for different empirical and physical models (Iyyani et al. 2015;

Zhang et al. 2016). Thus, spectral analysis alone leads to ambiguity in selecting the best fit model. One way forward is to have more constraining observables such as polarization, which can help to break this degeneracy (Toma et al. 2009; Covino & Gotz 2016; McConnell 2017; Gill et al. 2020, 2021). This is possible because different radiation models predict different ranges of polarization. For instance, one expects low to null polarization for photospheric emission while a wider range of polarization values is expected for synchrotron radiation, depending on the viewing geometry and magnetic field configurations present at the emission site (Granot & Königl 2003; Waxman 2003; Toma et al. 2009). Therefore, polarization measurements along with the spectrum could reveal a clearer picture of the underlying radiation mechanism. In addition, statistical studies of a large sample of GRB polarization values would help to assess the possible generic radiation model in GRBs.

In the last two decades, several hard X-ray spectrographs as well as dedicated X-ray polarimeters have contributed to polarization measurements of the GRB prompt phase. A summary of the GRB polarization measurements can be found in McConnell (2017), Chattopadhyay (2021), and Gill et al. (2021). However, statistically significant polarization measurements are available only for a handful of GRBs, and the obtained values exhibit a wide range. For example, the Gamma-ray Polarimeter (GAP, Yonetoku et al. 2011a) on board IKAROS provided polarization measurements for three bright GRBs (Yonetoku et al. 2011b, 2012). A high polarization fraction was reported for GRB 110301A ( $\sim 70\%$ ) and GRB 110721A ( $\sim 84\%$ ) in the full burst period, whereas, in the case of GRB 100826A, a flip in polarization angle was seen between two pulses. Recently, POLAR (Produit et al. 2018) provided precise polarization measurements for 14 GRBs (Zhang et al. 2019; Kole et al. 2020). These authors, however, reported a low level of polarization across the burst duration for a majority of the GRBs in their sample. For GRB 170114A, a temporal evolution of polarization was seen within the pulse (Burgess et al. 2019; Zhang et al. 2019). The Cadmium Zinc Telluride Imager (CZTI) on board AstroSat reported high polarization for most of the 11 bright GRBs detected in the first year of its operation (Chattopadhyay et al. 2019). Detailed spectropolarimetric analysis of some of these bright GRBs revealed time- and energy-dependent variation in polarization happening across the burst duration (Chand et al. 2018, 2019; Sharma et al. 2019, 2020). Most importantly, we note that the detailed study of GRB 160821A showed a  $\sim 90^\circ$  flip in polarization angle occurring twice within a single broad emission pulse (Sharma et al. 2019). Thus, the temporal evolution of polarization observed within the bursts GRB 160821A and GRB 170114A suggested that the prompt emission was highly dynamic, resulting in the dilution of the observed polarization measured across the total burst duration. Therefore, the existing polarization measurements indicated that the polarization in GRBs spans a wide range from low to high values. However, a preference toward low polarization values was observed in the sample and it would be interesting to classify them into cases of intrinsic low polarization or a concealed change in angle.

While POLAR stopped its scientific operations after 2017, CZTI on board AstroSat continues to work as a sensitive GRB monitor. Here, we present the polarization catalog for 20 bright GRBs that were observed in the first five years of operation of

CZTI (2015 October 6–2020 October 5). In this sample, besides selecting the GRBs with fluence higher than  $10^{-5}$  erg cm $^{-2}$ , we choose only those GRBs that were detected within the incident angle range of  $\sim 0^\circ$ – $60^\circ$  and  $\sim 120^\circ$ – $180^\circ$  in CZTI coordinates. The sample selection and the observed properties of the GRB sample are discussed in Section 2. We have also improved the GRB polarization analysis technique by including better noise rejection algorithms and by enhancing the polarimetric sensitivity at higher energies. The details of the data analysis and the new improvements are discussed in Section 3. In Section 4, we present the polarization results for the sample, and we follow with discussions in Section 5 and conclusions in Section 6.

## 2. The Five-year Sample of GRBs for Polarimetry

CZTI has been working as a prolific GRB monitor since the launch of AstroSat. In the five years selected for the present study, between 2015 October 6 and 2020 October 5, CZTI detected a total of 413 GRBs.<sup>12</sup> For polarization analysis, we selected 126 GRBs with fluence above  $10^{-5}$  erg cm $^{-2}$  in the energy range 10–1000 keV. The Fermi and Swift catalogs list 279 GRBs (41 GRBs are in common) above this fluence limit during the corresponding five-year period. Considering  $\sim 30\%$  of Earth occultation at any given time, and  $\sim 18\%$  of data gap due to passage through the South Atlantic Anomaly (SAA) or telemetry errors, detection of the bright GRBs in CZTI ( $\sim 44\%$ ) is mostly consistent with its effective duty cycle and sky coverage. However, we found that some fraction of far off-axis GRBs ( $>60^\circ$ ) are lost due to obscuration by other payloads, e.g., LAXPC, SXT, UVIT, and the spacecraft structures around CZTI. However, the detection rate is close to 100% for GRBs detected in the range  $0^\circ$ – $60^\circ$ , implying that the sample is complete in this angle range.

A subset of 77 GRBs in the list of 126 are detected in the angle ranges  $\sim 0^\circ$ – $60^\circ$  and  $\sim 120^\circ$ – $180^\circ$  in CZTI coordinates, which is required for polarization analysis (more details in Section 2.1). We also impose a minimum polarimetric sensitivity (MDP, or minimum detectable polarization) of 40% on the GRBs, based on the detected number of Compton scattered photons, which limits the final sample to 20 GRBs for polarization study.

### 2.1. Selection of GRBs

Pixelated CZT detectors with the ability to record ionizing events in neighboring pixels simultaneously can be used to identify Compton scattered events and hence are capable of measuring polarization properties of incoming radiation in the hard X-ray regime (above 100 keV). CZTI was calibrated with polarized on-axis sources before the launch of AstroSat (Chattopadhyay et al. 2014; Vadawale et al. 2015), thus demonstrating that subtle systematics involving reading data from neighboring simultaneous events are well understood and taken care of. For off-axis sources such as GRBs, it was assumed that we could use the physics of radiation interaction to extract the polarization information (Chattopadhyay et al. 2019). However, additional systematics could be present while using planar detectors to measure the scattering angles from off-axis sources. To particularly address these issues, we conducted an experimental study with a spare CZT detector

<sup>12</sup> <http://astrosat.iucaa.in/czti/?q=grb>.

module (identical to the one used in AstroSat-CZTI) to investigate the polarization sensitivity of CZTI to off-axis polarized radiation (C. S. Vaishnav et al. 2022 in preparation). The experiment was conducted with a partially polarized 190–240 keV continuum at various off-axis polar and azimuthal angles with respect to the CZT module to compare the measured polarized fraction with that of incident X-rays. Because of the complicated geometry and diverging X-rays, it was difficult to estimate the polarization fraction of the incident X-rays analytically. Hence we carried out Geant4 (Geometry and Tracking, Agostinelli et al. 2003) simulations of the complete experimental setup starting from the generation of a partially polarized source from unpolarized X-rays from the  $^{133}\text{Ba}$  source and estimated the polarization fraction of the X-rays incident on the detector by recording the electric field vector for each photon. We then analyzed the experimental and simulated data using the same techniques. We found that the measured polarization fractions from experiments and simulations agree with each other and with the incident polarization fraction within statistical uncertainties. For larger incidence angles ( $45^\circ$ – $60^\circ$ ), however, it was found that the assumption of approximating a divergent beam with a parallel beam could induce some experimental systematics, giving a slight mismatch between the estimated and original polarization (this should not be present in cosmic sources such as GRBs). At angles beyond  $\sim 60^\circ$  from the detector normal, polarization sensitivity is shown to be relatively low (i.e., MDP is high) compared to that for lower inclinations. These results helped fine-tune the methods of analyzing polarization, particularly the selection of GRBs for polarization analysis.

We used the  $\mu_{100}$  values (modulation amplitude for 100% polarized radiation) obtained from the Geant4 simulation of the AstroSat mass model to calculate MDP values for the GRBs from the known GRB and background count rates. A  $\sim 40\%$  limit on the MDP level was imposed to select the GRBs for polarization analysis. This criterion in most of the cases flags out the GRBs detected at off-axis angles between  $60^\circ$  and  $120^\circ$  and leaves 20 GRBs out of 77.

The list of the 20 GRBs and their observed properties is given in Table 1. In the first column under the name of the GRBs, we specify the instruments that were triggered. Fourteen of the GRBs have triggered Fermi/GBM detectors, seven of them have triggered Swift/BAT detectors, while two of them triggered both. There are four GRBs triggered in both Swift/BAT and Konus-Wind. There are two GRBs, GRB 200806A and GRB 190928A, that triggered only BAT and Konus-Wind, respectively. Localization information for GRB 190928A is available from the interplanetary network. The GRB location error circles quoted in the table are taken from Swift/XRT, Swift/BAT, and Fermi/GBM catalogs or the respective Gamma-ray Coordinates Network (GCN) Circulars. The last column of Table 1 shows the respective polar ( $\theta$ ) and azimuthal ( $\phi$ ) angles of detection in CZTI coordinates. It is to be noted that in Chattopadhyay et al. (2019) we reported polarization measurements for 11 bright GRBs from the first year of AstroSat. However, in this work, polarization analysis has been conducted only for six of those GRBs because the others were detected at far off-axis angles and do not satisfy the 40% MDP criterion.

## 2.2. Selection of Burst Interval

In this work, polarization analysis has been conducted for the time-integrated emission of the bursts. The burst interval

is chosen by employing a Bayesian block algorithm (Scargle 1998; Scargle et al. 2013; Burgess 2014) on the two-pixel Compton event light curves of the bursts (the definition of the Compton events and their selection are discussed in the next section). In Bayesian block analysis, the probability density corresponding to the background region is used to identify the start and stop times of the burst. The time stamp of the first block close to the burst with probability density greater than that of the background is considered as the start time of the GRB. The stop time is estimated in a similar way. The start and stop times ( $t_1$  and  $t_2$ ) for all the bursts and the burst duration used for polarization analysis are given in Table 1. For the GRBs detected by Fermi,  $t_1$  and  $t_2$  are given with respect to the GBM trigger times. For the remaining GRBs, the trigger times were taken either from Swift-BAT or Konus-Wind.

## 2.3. Spectroscopic Properties of the Sample

Knowledge of spectral energy distribution of the incoming photons is critical for modeling the interaction of the photons with the spacecraft, instrument supporting structures, and other payloads. The Geant4 platform is normally used to model these effects, given that the energy distribution of photons for a given GRB is known. To extract the spectral parameters for all the selected GRBs at the same time intervals as have been used for the polarization measurements, we carried out broadband spectroscopy using all the available data.

For the 13 GRBs (see Table 1) detected by GBM (we do not analyze GRB 160623A with GBM as the prompt emission was detected only partially at a later phase of the burst), the GBM time-tagged events were retrieved from the Fermi Science Support Center archives.<sup>13</sup> The photon spectra were fitted with a Band model (Band et al. 1993). For the six GRBs detected by Konus-Wind, we fitted Konus-Wind data with a Band function to estimate the spectral parameters (Svinkin et al. 2016; Tsvetkova et al. 2017, 2021). Since the typical accumulation time for a Konus-Wind spectrum is around 8 s, it is not possible to accumulate the data precisely in the selected time intervals. For spectral analysis, the closest time stamps to  $t_1$  and  $t_2$  were used (see footnote to Table 1). For GRB 200806A detected by BAT, we obtained the spectral parameters from BAT and CZTI data analysis. The background-subtracted BAT spectral files in the energy range 15–150 keV were extracted from the event file using the standard procedure.<sup>14</sup> Because of the limited energy window of the BAT spectral data, we used the CZTI spectral data that include the single-pixel events (100–900 keV), two-pixel Compton events (100–700 keV), and CsI-Veto events (100–500 keV) for a combined spectral analysis. The CZTI spectral files were generated and analyzed using the methodology described in Chattopadhyay et al. (2021). The obtained spectral parameters ( $\alpha$ ,  $\beta$ ) and peak energy ( $E_p$ ) are tabulated in Table 1. The quoted errors on the parameters are for the 90% confidence level. From the spectral parameters, we calculated the fluence in the selected time intervals in the 10–1000 keV band (given in the eighth column of the table). Values of the derived spectral parameters are consistent with those reported in the GCN Circulars and catalogs for the full burst interval.

<sup>13</sup> <https://fermi.gsfc.nasa.gov/ssc/data/access/>.

<sup>14</sup> [https://swift.gsfc.nasa.gov/analysis/threads/bat\\_threads.html](https://swift.gsfc.nasa.gov/analysis/threads/bat_threads.html).

**Table 1**  
Sample of GRBs Selected for Polarization Study with CZTI

GRB (Detectors)	Localization <sup>a</sup>	Burst Interval <sup>c</sup> (s)	( $t_1, t_2$ ) <sup>d</sup> (s)	$\alpha$	$\beta$	$E_p/E_c$ (keV)	Fluence <sup>c, e</sup> (10–1000 keV) ( $\times 10^{-5}$ erg cm <sup>-2</sup> )	Incident Direction ( $\theta, \phi$ ) (deg)
160325A (GBM, BAT)	1 <sup>h</sup> 7	43.82 (42.94)	(2.28, 46.10)	$-0.75^{+0.084}_{-0.070}$	$-1.97^{+0.100}_{-0.140}$	$223.57^{+29}_{-25}$	2.00 (1.86)	0.66, 159.48
160623A <sup>b</sup> (GBM, Konus-Wind)	3 <sup>h</sup> 5	17.05 (107.78)	(1.16, 18.21)	$-0.94^{+0.018}_{-0.020}$	$-2.83^{+0.090}_{-0.100}$	$662^{+19}_{-18}$	39.3 (0.39)	140.52, 118.09
160703A <sup>b</sup> (BAT, Konus-Wind)	3 <sup>h</sup> 9	24.91 (44.40)	(-1.78, 23.12)	$-0.78^{+0.120}_{-0.090}$	< - 2.48	$351^{+40}_{-46}$	2.02 (0.90)	10.15, 95.08
160802A (GBM)	1 <sup>h</sup> 0	18.07 (16.38)	(0.03, 18.11)	$-0.64^{+0.040}_{-0.030}$	$-2.53^{+0.140}_{-0.200}$	$207^{+1}_{-1}$	6.36 (6.84)	52.95, 273.12
160821A (GBM, BAT)	1 <sup>h</sup> 0	37.96 (43.01)	(117.18, 155.135)	$-0.96^{+0.003}_{-0.003}$	$-2.29^{+0.015}_{-0.015}$	$977^{+12}_{-12}$	48.1 (52.22)	156.18, 59.27
170527A (GBM)	1 <sup>h</sup> 0	37.95 (49.15)	(-0.76, 37.18)	$-0.99^{+0.011}_{-0.011}$	$-3.14^{+0.290}_{-0.290}$	$974^{+51}_{-47}$	8.36 (8.43)	26.54, 101.57
171010A (GBM)	1 <sup>h</sup> 4	99.06 (107.27)	(7.14, 106.20)	$-1.12^{+0.005}_{-0.002}$	$-2.39^{+0.024}_{-0.024}$	$180^{+3}_{-3}$	63.1 (63.28)	55.30, 35.19
171227A (GBM)	1 <sup>h</sup> 0	30.01 (37.63)	(0.26, 30.27)	$-0.80^{+0.011}_{-0.011}$	$-2.49^{+0.047}_{-0.049}$	$899^{+32}_{-32}$	26.8 (28.96)	146.49, 353.57
180103A <sup>b</sup> (BAT, Konus-Wind)	3 <sup>h</sup> 8	165.83	(11.38, 177.21)	$-1.31^{+0.060}_{-0.060}$	$-2.24^{+0.900}_{-0.130}$	$273^{+26}_{-23}$	22.3	52.33, 108.17
180120A (GBM)	1 <sup>h</sup> 0	24.01 (28.93)	(0.09, 24.10)	$-1.01^{+0.014}_{-0.014}$	$-2.40^{+0.090}_{-0.090}$	$140.91^{+3}_{-3}$	5.68 (6.45)	15.89, 206.28
180427A (GBM)	1 <sup>h</sup> 0	13.01 (25.92)	(0.15, 13.16)	$-0.29^{+0.077}_{-0.077}$	$-2.80^{+0.160}_{-0.160}$	$147^{+2}_{-2}$	4.34 (5.04)	40.81, 257.79
180806A (GBM)	5 <sup>h</sup> 0	10.33 (15.62)	(-0.01, 10.32)	$-0.92^{+0.039}_{-0.036}$	$-2.46^{+0.230}_{-0.440}$	$453^{+46}_{-44}$	1.78 (2.24)	26.79, 246.11
180809B <sup>b</sup> (BAT, Konus-Wind)	1 <sup>h</sup> 4	63.00 (233.20)	(-3.89, 59.11)	$-0.69^{+0.080}_{-0.070}$	$-2.29^{+0.070}_{-0.080}$	$251^{+16}_{-15}$	23.6 (7.30)	61.44, 17.49
180914A (GBM)	5 <sup>h</sup> 0	128.01 (122.37)	(5.34, 133.35)	$-0.73^{+0.032}_{-0.031}$	$-2.30^{+0.110}_{-0.150}$	$330^{+20}_{-19}$	9.76 (8.19)	52.92, 173.40
180914B <sup>b</sup> (BAT, Konus-Wind)	3 <sup>h</sup> 4	170.04	(-13.81, 156.23)	$-0.75^{+0.040}_{-0.040}$	$-2.10^{+0.080}_{-0.700}$	$453^{+26}_{-24}$	59.8	36.45, 314.92
190530A (GBM)	1 <sup>h</sup> 4	26.86 (18.43)	(7.24, 34.10)	$-0.99^{+0.022}_{-0.002}$	$-3.50^{+0.250}_{-0.250}$	$888^{+8}_{-8}$	38.5 (37.06)	154.50, 79.87
190928A <sup>b</sup> (Konus-Wind)	2 <sup>h</sup> 1	119.97	(-2.70, 117.26)	$-1.00^{+0.060}_{-0.060}$	$-1.97^{+0.070}_{-0.130}$	$658^{+111}_{-88}$	20.5	57.69, 231.26
200311A (GBM)	1 <sup>h</sup> 0	39.07 (52.48)	(0.14, 39.20)	$-0.95^{+0.020}_{-0.020}$	$-2.57^{+0.190}_{-0.190}$	$1218^{+110}_{-110}$	114 (4.25)	29.89, 151.24
200412A (GBM)	1 <sup>h</sup> 4	14.17 (12.61)	(-0.89, 13.28)	$-0.70^{+0.050}_{-0.050}$	$-2.50^{+0.210}_{-0.210}$	$256^{+8}_{-7}$	3.24 (2.87)	41.57, 272.66
200806A (BAT)	1 <sup>h</sup> 7	38.04 (38.80)	(-2.85, 35.18)	-0.53	-2.96	109.12	2.44 (0.10)	6.78, 262.58

**Notes.**

<sup>a</sup> Localization given with 90% error radius, taken from Swift/XRT, Swift/BAT, and Fermi/GBM catalogs. For GRB 190928A, localization information is available from IPN.

<sup>b</sup> Spectral parameters obtained from Konus-Wind for the following burst intervals: 1, GRB 160323A: 18.176 s; 2, GRB 160703A: 24.832 s; 3, GRB 180103A: 169.984 s; 4, GRB 180809B: 64.256 s; 5, GRB 180914B: 160.000 s; 6, GRB 190928A: 119.808 s.

<sup>c</sup> The values inside the parenthesis are the T90 and fluence values in the Burst Interval and Fluence columns, respectively, as reported in the IceCube catalog [https://user-web.icecube.wisc.edu/~grbweb\\_public](https://user-web.icecube.wisc.edu/~grbweb_public).

<sup>d</sup>  $t_1$  and  $t_2$  are with respect to GBM/BAT/Konus-Wind trigger time.

<sup>e</sup> Fluence is in the range  $t_1$ - $t_2$  at 10–1000 keV.

### 3. Methodology of GRB Polarimetry with CZTI

CZTI consists of an array of 64 CZT detector modules where each detector is 5 mm thick and spatially segmented into 256 pixels (with a nominal pixel size of  $2.5 \text{ mm} \times 2.5 \text{ mm}$ ). The availability of photon tagging mode in CZTI (time resolution of  $20 \mu\text{s}$ ) and a significant Compton scattering cross section beyond 100 keV enable CZTI to work as a sensitive Compton polarimeter. Vadawale et al. (2018) reported the measurement of polarization of the Crab pulsar and nebula using CZTI in the 100–380 keV energy band. Later, using the same principle, polarization measurement for a sample of GRBs was reported by Chattopadhyay et al. (2019), where the details of the method are also presented. Here we briefly summarize the steps.

1. We identify the adjacent two-pixel events from the  $20 \mu\text{s}$  coincidence window.
2. We demand that the ratio of the energies deposited in two adjacent pixels is between 1 and 6 to filter out the background and noisy events. A Geant4 simulation study shows that the signal-to-noise ratio is optimum in this range.
3. These steps are applied on both the burst region obtained from the Bayesian block analysis on the GRB light curves (see Section 2.2) and at least 300 s of pre-burst and post-burst background intervals. For each valid event, we estimate the azimuthal scattering angle. The azimuthal angle distribution from the list of valid events in the background region is subtracted from that in the GRB region.
4. An unpolarized azimuthal angle distribution is then used to correct the background-subtracted azimuthal distribution for the inherent modulation that is seen even for fully unpolarized radiation (Chattopadhyay et al. 2014). The square pixels in the CZTI detector plane introduce an asymmetry in the scattering geometry that causes the observed inherent modulation. The unpolarized distribution is obtained from the AstroSat mass model (Mate et al. 2021) by simulating  $10^9$  unpolarized photons in Geant4 with source photon energy distribution the same as the GRB spectral distribution (modeled as a Band function) and for the same orientation with respect to the spacecraft.

The corrected azimuthal angle distributions are then fitted with a sinusoidal function to calculate the modulation amplitude ( $\mu$ ) and polarization angle in the detector plane ( $\phi_0$ ) using the Markov Chain Monte Carlo (MCMC) method. There is an alternative method (“template fitting method”) where the raw histograms can be fitted with templates generated from simulations. The modulation curve-fitting method assumes a cosine nature of the azimuthal distributions, which is not strictly true at larger angles, particularly when the distributions have high counting statistics. The off-axis experiment with CZTI detectors (C. S. Vaishnav et al. 2022, in preparation) shows that modulation curve fitting provides the same results as template fitting even for Compton events, which are typically a factor of ten more numerous than GRBs. Modulation curves help visual representation, and since the same method has been used in earlier analysis, we continue with the standard sinusoidal method in this work for consistency.

Polarization fraction is obtained by normalizing the fitted  $\mu$  with  $\mu_{100}$ , where  $\mu_{100}$  values are obtained by simulating the

AstroSat mass model in Geant4 for 100% polarized radiation ( $10^9$  photons) for the same GRB spectral distribution and orientation. For each GRB, we calculate the Bayes factor for confirmation of detection of polarization. For GRBs with Bayes factor  $< 3$ , we estimate upper limits in polarization. Details of the Bayes factor and calculations of upper limits are given in Chattopadhyay et al. (2019).

#### 3.1. New Improvements in the Analysis

There are some new developments in the CZTI polarimetry analysis, particularly in case of GRBs, that improve the overall polarimetric sensitivity of CZTI and help in taking care of the systematic effects. Here we discuss these new developments briefly.

##### 3.1.1. Extending the Polarimetry Energy Range to 600 keV

Recently, in Chattopadhyay et al. (2021), we discussed calibration of a fraction of CZTI pixels (around 20%) that were found to have lower gains from onboard calibration soon after the launch of AstroSat (we will refer to these pixels as low-gain pixels hereafter). Because of lower gains, these pixels have a higher energy threshold of  $\sim 60$  keV for X-ray photon detection but are also sensitive to photons of much higher energies up to  $\sim 1$  MeV. We used five years of CZTI background data to calibrate these low-gain pixels using high-energy particle-induced tellurium activation lines at 88 keV and 145 keV (Odaka et al. 2018) and by comparing the count distribution between the low-gain and the normal-gain CZTI pixels. The low-gain pixels were thereafter successfully utilized in the CZTI analysis software to obtain single-pixel spectra and two-pixel Compton spectra at  $\sim 100$ – $1000$  keV for a sample of 11 bright GRBs (for details, see Chattopadhyay et al. 2021). We also did not see any variation in gain of these pixels over time. Here we explore the possibility of using the low-gain pixels in extracting polarization information. Use of the low-gain pixels enhances the signal-to-noise ratio of the signal because of the availability of additional collecting area. However, these additional events (combination of two low-gain pixels or one low-gain and one normal-gain pixel) are mostly associated with high-energy photons, and at those energies the distinction between the first event (scattering of the incident photon) and second event (subsequent absorption of the scattered photon) can sometimes be difficult because for incident photon energies  $> 260$  keV, more energy can be deposited in the first event than in the second for some of the scattering angles.

We attempt to address this problem using Compton kinematics and Monte Carlo simulations. From the known Compton kinematics formulation, for each observed Compton event, we first calculate  $\theta_{\text{critical}}$  for  $E_{\text{total}} (= E_{\text{low}} + E_{\text{high}}) > 260$  keV, such that the scattered photon energy or the energy deposited in the second event is lower than the electron recoil energy or the energy deposited in the first event. This is followed by the calculation of the polar angle of scattering ( $\theta$ ) from  $E_{\text{total}}$  assuming that  $E_{\text{low}}$  is the scattered photon energy or the energy deposited in the second event. If  $180^\circ > \theta > \theta_{\text{critical}}$ , we calculate the probability of such a scattering scenario by integrating the Compton scattering cross section from  $\theta$  to  $180^\circ$ . If the probability is high ( $> R[0, 1]$ , a random number drawn from a uniform distribution between 0 and 1), the low-energy deposition is classified as the second event and used to calculate the azimuthal angle of scattering

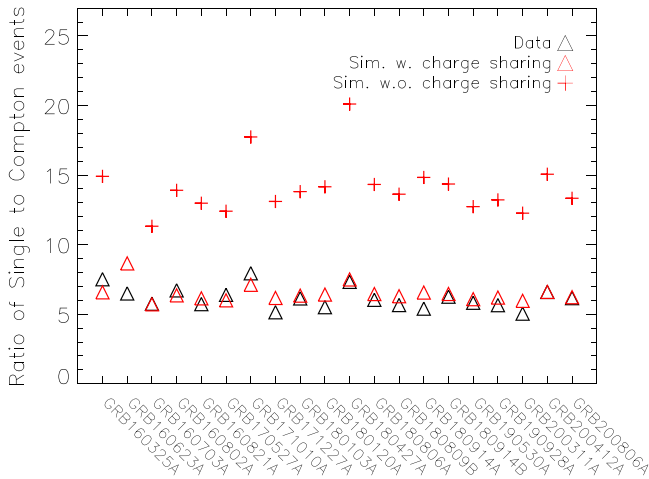


**Figure 1.** Comparison of the ratio of single to Compton events from observed data and simulation. The observed data points are shown as black triangles. If we do not include charge sharing in the simulation, simulated ratios (red crosses) are a factor 2 higher. However, after correction for charge sharing, the simulated values shown by red triangles agree closely with the observed values.

correctly. Although the low-gain pixels are sensitive to very high energies, here we impose a 600 keV limit because the polarization analyzing power (represented by  $\mu_{100}$ ) of CZTI or CZTI-like Compton geometry decreases significantly at higher energies.

### 3.1.2. Improvement in Noise Rejection

There is an ongoing effort to improve upon the existing noise rejection algorithms for CZTI. Ratheesh et al. (2021) summarize the new improvements in the background and noise rejection methods. One of the important developments, particularly for the polarization analysis, is the implementation of a “Compton noise” algorithm. Some of the adjacent noisy pixels flickering on a timescale of less than  $20 \mu\text{s}$  are seen to filter into the Compton event list and cause systematic artifacts in the azimuthal angle distribution. In the new noise rejection algorithm, we identify these events in the histogram of the two-pixel Compton detector plane as outliers and filter them out with a user-defined outlier level ( $n\sigma$ ). This is carried out separately for the edge and the corner pixels. Further details on the Compton noise analysis can be found in Ratheesh et al. (2021). We generate the Compton event list for all 20 GRBs after applying the two-pixel noise correction.

### 3.1.3. Effect of Charge Sharing in CZTI

In a pixelated detector like CZTI, where the pixels are defined by the anode pattern, it is likely that any charge deposited close to the pixel boundary is shared between two adjacent pixels. The effect of such charge sharing is expected to increase at higher energies because of longer track lengths of the high-energy electrons resulting in a larger radius of the charge cloud. Charge-sharing events in which the leaked charge is above the energy threshold of the neighboring pixel result in double-pixel events and can mimic a Compton event. The effect of charge sharing can be seen in Figure 1, where we compare the ratio of single-pixel events to two-pixel Compton events seen in the observed data and Geant4 simulations separately at 100–600 keV for all 20 GRBs. The ratios obtained from simulation (shown by red crosses) are consistently higher than the observed values (black triangles). We try to verify that

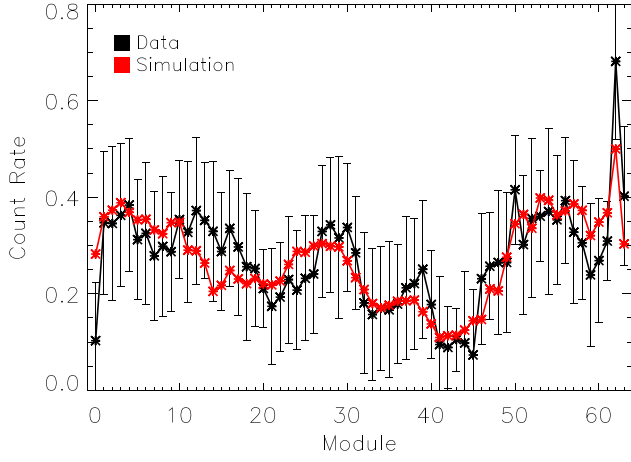
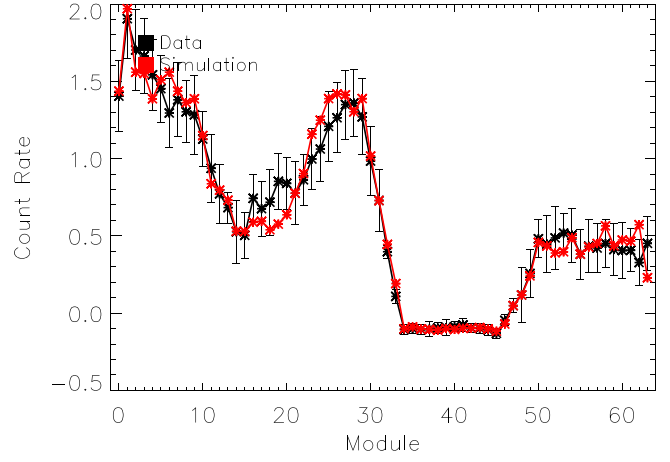
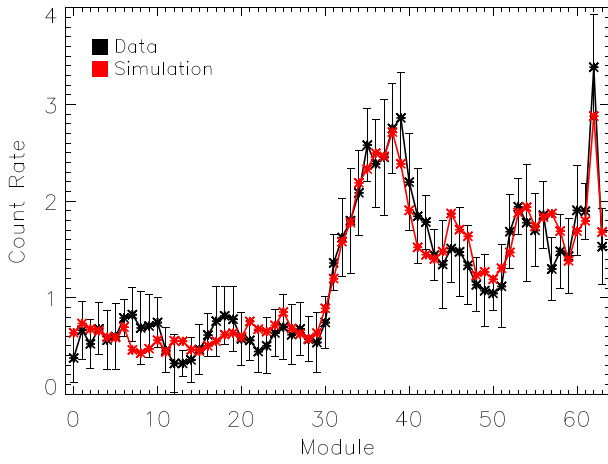
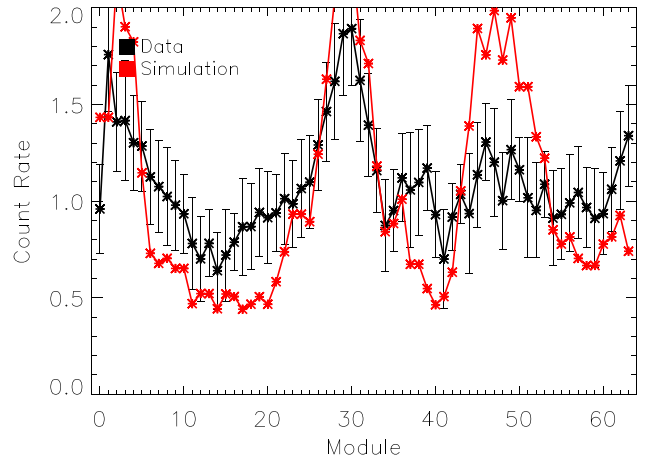
this difference is a result of charge sharing by estimating the area of the charge-sharing region in each pixel and use that fractional area ( $f$ ) to correct the number of single-pixel ( $N_{\text{single}} - f \times N_{\text{single}}$ ) and two-pixel Compton events ( $N_{\text{Compton}} + f \times N_{\text{Compton}}$ ). This fractional area is estimated from the size of the charge cloud at the electrode, which in turn is calculated from the detector depth, charge drift distance, detector substrate bias, and temperature (CZTI charge-sharing calculations are given in detail in Chattopadhyay et al. 2016). The final radius of the charge cloud also depends on its initial radius, which is normally approximated as the range of the photoelectron. For that, we calculate the weighted range of photoelectrons in CZT for the known power-law spectra of the GRBs.

In the azimuthal angle distributions, the effect of charge sharing artificially increases the number of edge double pixels compared to corner double pixels, because in the case of sufficient charge leaking into the adjacent corner pixel, at least one (or possibly two) adjacent edge pixels will get a higher charge, and hence such an event will get registered as a three- or four-pixel event and thus will be rejected during the Compton event selection. Since the azimuthal histograms obtained by Geant4 simulations are used for geometric corrections of the observed azimuthal histograms, it is necessary to correct for the charge sharing, which is done by normalizing the ratio of edge to corner pixels for the Geant4 simulations to that of the observed data. This correction is applied before the geometric correction, and thus preserves the polarization-induced modulation within the edge and corner pixels. We used the same method in experimental analysis and found the results to agree well (C. S. Vaishnav et al. 2022, in preparation).

### 3.1.4. Improvements and Validation of the AstroSat Mass Model

Polarization for off-axis sources with CZTI critically depends on the accuracy of the mass model of AstroSat. In order to understand the effect of the surrounding material on unpolarized and polarized radiation, we modeled the entire AstroSat observatory inside Geant4 including all the payloads of AstroSat: SSM, UVIT, SXT, LAXPC, CZTI, and the satellite bus. In our previous GRB polarimetry paper (Chattopadhyay et al. 2019) we discussed the basic concepts in the development of the mass model and its validation using observed data for GRB 160821A. In recent times, we made a number of changes in the mass model geometries based on the feedback from observed data, particularly in the CZTI housing and the spacecraft. These details along with the development of the complete AstroSat mass model in Geant4 can be found in Mate et al. (2021). In Chattopadhyay et al. (2021), we performed broadband spectroscopy for a sample of GRBs using CZTI single-pixel and two-pixel Compton events and using response matrices obtained from Geant4 simulations of the mass model interactions. The spectroscopic results closely agree with the Fermi parameters, which validates the mass model.

The validation of the mass model using a large sample of GRBs by comparing the simulated and observed detector plane histograms (DPHs) of single-pixel events at 70–200 keV is also attempted in Mate et al. (2021). It was found, however, that the simulation could not fully replicate all the observations, perhaps due to the fact that the single events contain low-energy photons that have leaked through small gaps (which

(a) GRB 160325A:  $\theta = 0.66^\circ$ ,  $\phi = 159.48^\circ$ (b) GRB 170527A:  $\theta = 26.54^\circ$ ,  $\phi = 101.57^\circ$ (c) GRB 180427A:  $\theta = 40.81^\circ$ ,  $\phi = 257.79^\circ$ (d) GRB 190530A:  $\theta = 154.50^\circ$ ,  $\phi = 79.87^\circ$ 

**Figure 2.** Comparison between observed (black) and simulated (red) detector plane histograms of two-pixel Compton events binned at module level for a sample of GRBs.

could not be adequately modeled), along with the scattered photons. Hence, in order to validate the mass model further, particularly in the context of polarization analysis, here we attempt to compare the simulated DPHs with the observed DPHs generated from the same Compton events that are used in polarization analysis. The analysis was performed for all 20 GRBs reported in the present work using Geant4 simulations. The simulation is done for a large number of photons ( $10^9$ ) with the same spectral energy distribution as observed for the GRBs. In the simulation, we implement the observed lower-level and upper-level discriminators of the CZTI pixels including the low-gain pixels. When the surrounding material and the spacecraft see an incoming photon, the outgoing energy and direction of the photon depend on its initial energy and momentum direction. We generated DPHs for all 20 GRBs in multiple energy bands and found that the simulated and observed DPHs for all the GRBs are found to agree well in all the energy bands. Figure 2 shows the observed and simulated module-wise DPHs for a sample of representative GRBs in the 100–600 keV band.

#### 4. Results

For time- and energy-integrated polarization, the Compton events in the full burst interval in the complete energy range of 100–600 keV are used. The background-subtracted and geometry-corrected azimuthal angle distribution of the valid Compton events is fitted with a sinusoidal function,  $A \cos 2(\phi - \phi_0 + \pi/2) + B$ , where  $A$  and  $B$  determine the modulation amplitude of the signal,  $\mu = A/B$ , and  $\phi_0$  is the polarization angle in the detector plane. To estimate the fitting parameters ( $A$ ,  $B$ ,  $\phi_0$ ) and the associated errors, we perform MCMC simulations for a large number (1 million) of iterations. For each iteration, the posterior probability is estimated based on randomly sampled model parameter values. Figure 3 shows the posterior probability distribution for  $\mu$  (bottom right plot) and polarization angle in the detector plane,  $\phi_0$  (middle left plot) for one of the bursts, GRB 180103A.

The 1 s light curve and the selected region (based on Bayesian block analysis, see Section 2) are shown in the top panel of the figure. The 8-bin modulation curve after background subtraction and geometric correction along with

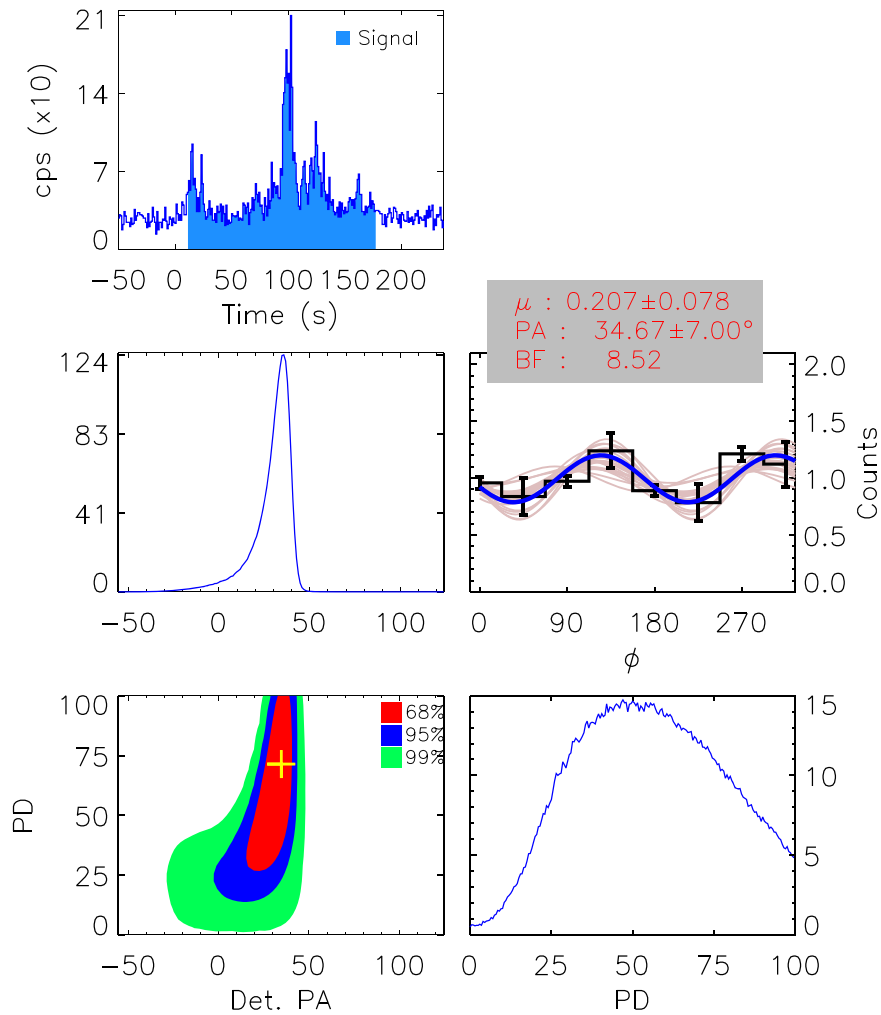


**Figure 3.** Modulation curve for GRB 180103A. Top: 1 second Compton light curve at 100–600 keV. The Compton events for polarization analysis are obtained from the blue shaded region. Middle left: posterior probability distribution for polarization angle from MCMC iterations. Middle right: the modulation curve and the sinusoidal fit shown as a solid blue line, along with 100 random MCMC iterations. Bottom left: the contour plot for polarization angle and degree for 68%, 95%, and 99% confidence levels. Bottom right: posterior probability distribution for polarization degree from MCMC iterations. Similar figures are given for the remaining 19 GRBs in the online journal.

(The complete figure set (20 images) is available.)

the sinusoidal fit (solid blue line) is shown in the middle right plot. We also show a distribution of the sinusoidal fits for 100 random iterations as solid pink lines. The 68%, 95%, and 99% contours for polarization fraction and angle for GRB 180103A are shown in the bottom left plot of Figure 3 in red, blue, and green, respectively.

In order to claim that the burst is truly polarized, we estimate the Bayes factor for the sinusoidal model ( $M_1$ , for polarized photons) and a constant model ( $M_2$ , unpolarized photons) as the ratio of the marginal likelihoods of  $M_1$  and  $M_2$  (for more details, see Chattopadhyay et al. 2019). For the GRBs with a Bayes factor greater than 3, we estimate polarization fraction and angle from the fitted parameters. For example, for GRB 180103A, the Bayes factor is found to be 8.35, implying that the signal is truly polarized and the probability of unpolarized radiation mimicking such sinusoidal modulation in the azimuthal angle distribution is low ( $<0.1\%$ , see Chattopadhyay et al. 2019, for details of chance probability calculations). Polarization fraction is estimated by normalizing the fitted modulation amplitude,  $\mu$ , by a modulation factor for 100%

polarized radiation ( $\mu_{100}$ ), which is calculated by simulating the AstroSat mass model in Geant4. Table 2 summarizes the results for all 20 GRBs.<sup>15</sup> The estimated Bayes factors are given in the third column of the table. We see that besides GRB 180103A, four other GRBs (GRB 180120A, GRB 180427A, GRB 180914B, and GRB 190530A) have a Bayes factor above 3 for which polarization fractions are estimated (fourth column). The fitted polarization angles in the CZTI and in the sky plane (north to east in an anticlockwise direction) are given in the fifth and sixth columns of Table 2, respectively, for these five GRBs. In the second column, we give the number of selected Compton events in the full burst intervals of the GRBs.

It is to be noted that the uncertainties quoted in Table 2 on polarization fraction and angle are obtained at 68% confidence level for only one parameter of interest, that is by looking only at the variation in the azimuthal angle distribution rather than the measurement of both polarization fraction and angle simultaneously. The latter is resorted to while determining

<sup>15</sup> Full data set and analysis techniques would be made available on reasonable request to the author.



**Table 2**  
Measured Polarization Fractions (PF) and Position Angles (PA) for the GRBs in the Energy Range 100–600 keV

GRB Name	$N_{\text{Compton}}$	Bayes Factor	PF (%) <sup>a</sup>	CZTI PA (deg) <sup>b</sup>	Sky PA (deg)
GRB 160325A	764	1.72	<45.02	...	...
GRB 160623A	1714	1.02	<56.51	...	...
GRB 160703A	433	0.76	<62.64	...	...
GRB 160802A	1511	0.69	<51.89	...	...
GRB 160821A	2851	0.87	<33.87	...	...
GRB 170527A	1638	0.79	<36.46	...	...
GRB 171010A	3797	0.98	<30.02	...	...
GRB 171227A	1249	0.84	<55.62	...	...
GRB 180103A	4164	8.52	$71.43 \pm 26.84$	$34.67 \pm 7.00$	122.13
GRB 180120A	705	3.95	$62.37 \pm 29.79$	$-3.65 \pm 26.00$	61.21
GRB 180427A	986	9.25	$60.01 \pm 22.32$	$16.91 \pm 23.00$	47.22
GRB 180806A	555	0.86	<95.80	...	...
GRB 180809B	3294	0.98	<24.63	...	...
GRB 180914A	2276	1.2	<33.55	...	...
GRB 180914B	7765	3.52	$48.48 \pm 19.69$	$26.99 \pm 19.00$	68.41
GRB 190530A	1859	3.08	$46.85 \pm 18.53$	$43.58 \pm 5.00$	154.05
GRB 190928A	4492	1.77	<33.10	...	...
GRB 200311A	1082	0.86	<45.41	...	...
GRB 200412A	911	0.89	<53.84	...	...
GRB 200806A	534	0.71	<54.73	...	...

#### Notes.

<sup>a</sup> The upper limits are calculated at the  $2\sigma$  level and the error bars are at the  $1\sigma$  level for the one parameter of interest.

<sup>b</sup> The error bars are at the  $1\sigma$  level for the one parameter of interest.

the contours. For the remaining 15 GRBs with Bayes factor  $<3$ , we calculate upper limits in polarization fraction by estimating the polarization detection threshold. The polarization detection threshold is determined by limiting the probability of false detection, which is estimated by simulating unpolarized incident radiation in Geant4 using the AstroSat mass model for the observed Compton and background events for a given GRB. The method of upper limit estimation is described in Chattopadhyay et al. (2019).

From Table 2, we see that only 25% of the sample is polarized according to the convention that the signal is polarized if the Bayes factor is greater than 3. The polarization level ranges between  $\sim 50\%$  and  $70\%$ . For a significant fraction of GRBs, the  $2\sigma$  upper limits on polarization are below  $40\%$ , signifying that most of the GRBs are unpolarized or polarized at a low level. It is to be noted that since the upper limit or the false detection probability is also estimated by looking only at the variation in the azimuthal angle distribution for unpolarized radiation, for certain bursts we still obtain meaningful upper limits on polarization fraction, even though the polarization contours are unconstrained at the  $68\%$  level.

## 5. Discussions

In this work, we have presented the results of a comprehensive analysis of the GRBs detected by CZTI on board the AstroSat satellite and have given the hard X-ray polarization results for 20 GRBs. In this section, we compare these results with those obtained by POLAR (Kole et al. 2020). We also discuss the implications of our polarization results in terms of the emission mechanism of the prompt bursts and generic features of GRB prompt emission polarization. We summarize the improvements that we have made in the polarization analysis technique and sketch possible future improvements and observation strategies.

### 5.1. Comparison with POLAR Results

Kole et al. (2020) using POLAR reported low polarization for time-integrated emissions of a sample of 14 GRBs, with only two GRBs having polarization fraction above  $40\%$ . In Chattopadhyay et al. (2019), we reported polarization measurements for a sample of 11 bright GRBs detected in the first year of AstroSat. However, these measurements were not carried out in the full burst interval of the GRBs, rather the selection of the intervals and the energy range were optimized to obtain the best detection of polarization. Most of the GRBs were found to have high polarization. In this work, however, polarization analysis has been done systematically for the full burst duration at 100–600 keV for all the GRBs in the sample. Since both POLAR and CZTI measurements reported here are carried out for the full burst intervals, we expect similar polarization properties in both cases. Two out of 14 POLAR GRBs were reported to have polarization above  $40\%$ , which translates to  $14\%$  of the sample. In the case of CZTI, for five GRBs the polarization fraction and angles were constrained with polarization fraction above  $\sim 50\%$ , implying that around  $25\%$  of the GRBs are polarized.

We used the reported polarization fraction values for the POLAR GRBs and the associated  $1\sigma$  errors from Table 2 of Kole et al. (2020) and computed the cumulative probability of polarization fraction. This is shown in Figure 4 in blue along with the  $1\sigma$  error boundaries. A similar distribution of cumulative probability of polarization fraction for the CZTI GRB sample is shown in gray. Each distribution is computed from randomly sampled values drawn from a Poisson distribution around the estimated polarization fraction with the error on the fraction as the standard deviation for the GRBs with Bayes factor above 3. In the case of GRBs with Bayes factor less than 3, we randomly sample a uniform distribution between 0 and the respective polarization upper limits. In order to avoid any bias in the sample, we select only the GRBs with

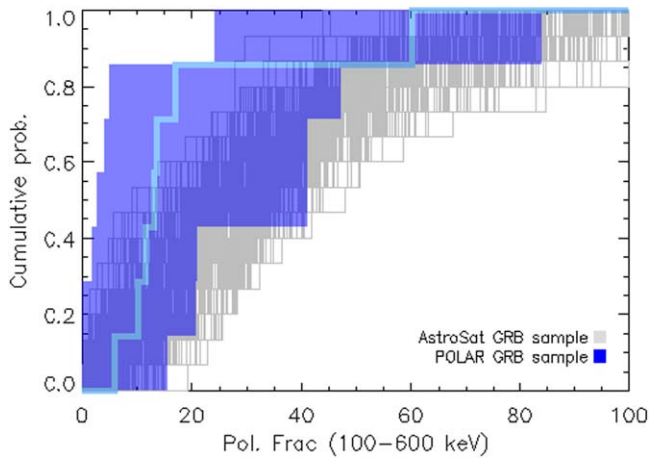


**Figure 4.** Comparison of POLAR and CZTI polarization results. The cumulative distribution of polarization fractions reported by POLAR for seven GRBs with fluence above  $10^{-5}$  erg cm $^{-2}$  (10–1000 keV) is shown by a solid blue line with  $1\sigma$  error boundary. The gray lines are obtained from 15 GRBs detected by CZTI with fluence above  $10^{-5}$  erg cm $^{-2}$  (10–1000 keV) and at angles less than  $60^\circ$  (see text for more details).

fluence above  $10^{-5}$  erg cm $^{-2}$  in the 10–1000 keV band for both POLAR and CZTI. In addition to that, for CZTI we selected the GRBs that are detected at incident angles  $\lesssim 60^\circ$  because the sample is complete in this angle range (see discussion in Section 2). We see that CZTI and POLAR show a similar distribution of polarization fraction such that 50% of the observed GRBs show a polarization fraction  $< 50\%$  of the peak value. There is, however, some discrepancy in the detected polarization fraction such that either POLAR polarization fractions are systematically lower by around 25% or CZTI values are systematically higher by around 25%. We expect a certain level of systematic error associated with both POLAR and CZTI or any polarimetry instrument in general. However, CZTI (or POLAR) known (or identified) instrumental systematics alone are unlikely to cause a discrepancy of 25%. We note that POLAR samples a wider time range because of its high sensitivity down to 50 keV. CZTI, on the other hand, being highly sensitive in the higher energy range above 100 keV, gives a snapshot picture of the narrow peak at high energy. We quantified this by conducting Bayesian block analysis for the 13 GRBs detected by both CZTI and Fermi at 50–500 keV, the energy range where POLAR is sensitive. We found that the estimated burst intervals are around a factor of 2 higher at 50–500 keV than those estimated at 100–600 keV, similar to the figure estimated in CZTI. GRB prompt emission is highly structured, leading to possible changes in the polarization angle within a burst, which has been seen for a number of GRBs, e.g., GRB 160821A (Sharma et al. 2019), GRB 170114A (Zhang et al. 2019), and GRB 100826A (Yonetoku et al. 2011b). Thus, we surmise that the sampling of longer time intervals by POLAR may have led to the dilution of the polarization fraction across the burst duration, in comparison to the shorter time intervals sampled by CZTI.

We have also attempted polarization measurement for GRB 161218B, which was detected by both CZTI and POLAR. Because the GRB is faint, POLAR could not constrain the polarization parameters. POLAR reported a polarization degree,  $PD = 13_{-13}^{+28}\%$  and sky polarization angle,  $PA = 68_{-54}^{+36}^\circ$  (Kole et al. 2020). The incident direction of GRB 161218B in CZTI was  $\theta = 121^\circ.63$ ,  $\phi = 117^\circ.71$ . For the

polarization and spectral analysis of GRB 161218B with CZTI, we chose the same region of the burst as selected by POLAR for polarization analysis with a burst interval around 25.1 s. The number of Compton counts in the burst duration was found to be 418 (below our selection criterion for inclusion in the five-year sample). We performed the standard polarization analysis for this GRB and found the Bayes factor to be low, consistent with zero polarization (in agreement with the POLAR result).

## 5.2. Correlation between Polarization and Spectral Parameters

Different radiation models for the prompt emission of GRBs predict different ranges of possible polarization fractions depending on the configuration of magnetic fields at the emitting site, the viewing geometry, and the jet structure (see Figure 1 in Gill et al. 2021). It is not possible to spatially resolve the emitting region, and thereby the observed polarization measurement is always an average of the radiation coming from the visible emitting region.

Synchrotron emission produced from a distribution of electrons is intrinsically linearly polarized. However, depending on the configuration of magnetic field within the  $1/\gamma$  view cone ( $\gamma$  being the bulk Lorentz factor of the jet), the average observed polarization can vary. Viewed within the jet opening angle  $\theta_j$ , a random orientation of the magnetic field would always produce low to null polarization and so will an azimuthally ordered magnetic field if the view axis coincides with the jet axis (Toma et al. 2009). The latter magnetic geometry, however, may produce significant polarization, between 16% and 70%, for spectral slope  $\alpha$  in the range  $-0.67$  to  $-1.5$  and off-axis view geometry with  $y_j \equiv (\gamma\theta_j)^2$  equal to 1 or higher for a top-hat jet (Granot & Königl 2003). On the other hand, photospheric emission, primarily resulting from Compton scattering, would exhibit little polarization within  $\theta_j$  (Toma et al. 2009). View angles outside the jet cone can lead to high observed polarization due to emission zone asymmetry (Granot & Königl 2003; Toma et al. 2009; Lundman et al. 2014), but in such cases the observed flux would be much lower and may preclude the measurement of polarization. In the case of subphotospheric dissipation too the observed emission can be polarized, but only at energies much below the spectral peak (Lundman et al. 2018).

The population properties of GRB polarization can also act as a possible discriminator between emission models. Toma et al. (2009) demonstrate that for synchrotron emission in ordered magnetic fields, a negative correlation between polarization fraction (PF) and spectral peak energy ( $E_{\text{peak}}$ ) may be expected, while this is not so in other emission models. With this in mind, we have plotted the measured PF and upper limits (100–600 keV) of our GRB sample against the observed  $E_{\text{peak}}$  in Figure 5, color-coded according to the estimated 10–1000 keV burst flux. Well constrained PF values are obtained for five cases, with PF lying in the range  $\sim 28\%$ – $97\%$  as per the confidence interval of one parameter of interest. These bursts have fluence values among the highest observed, which suggests that they are likely viewed within the jet opening angle. If so, then the strong observed polarization would prefer synchrotron emission in ordered magnetic fields as the main radiation mechanism. However, to confirm this assessment via a PF– $E_{\text{peak}}$  correlation, one would require a larger sample of GRBs than we currently have.

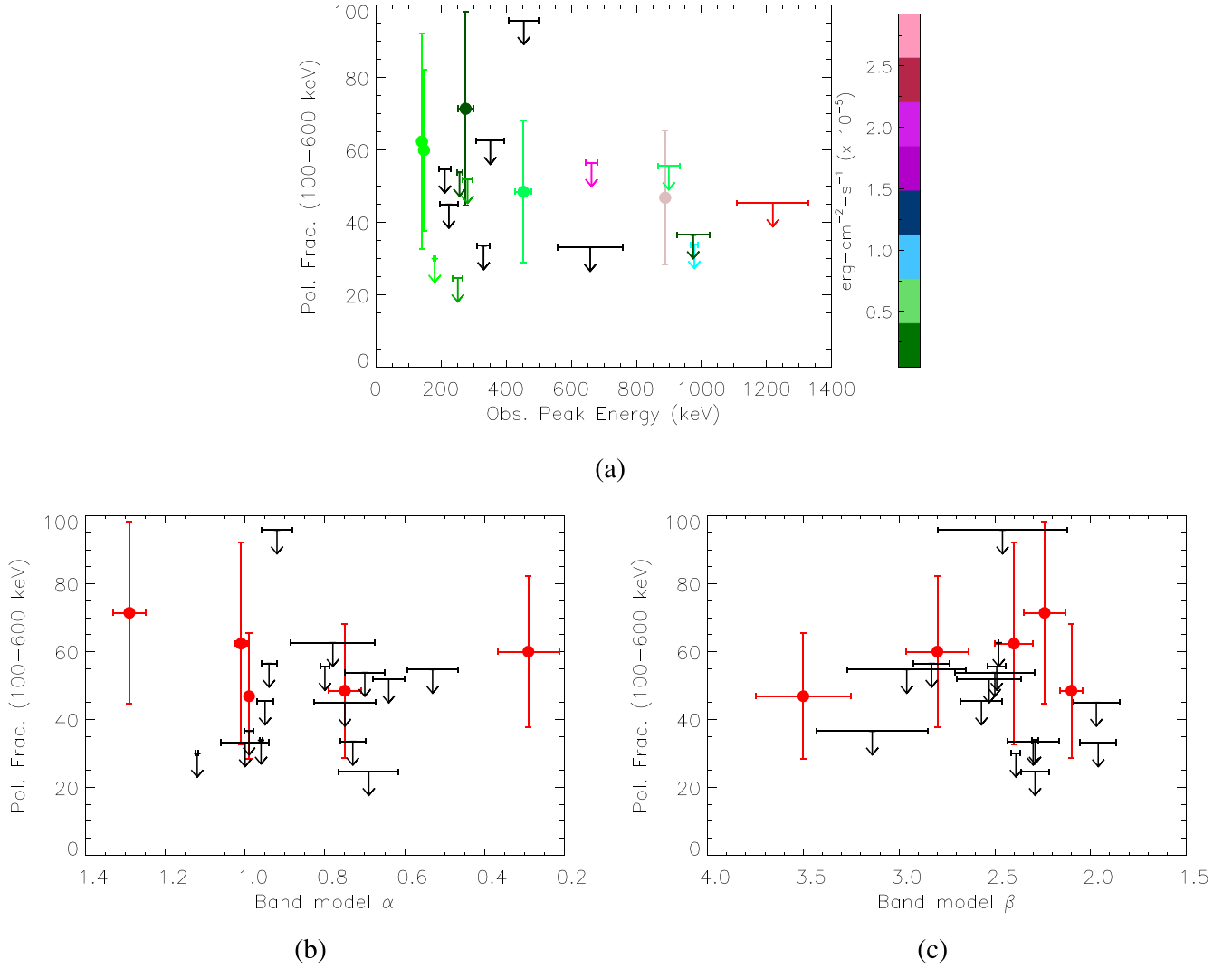


**Figure 5.** (a) Polarization fraction of the GRBs as a function of peak energy,  $E_{\text{peak}}$ . The 10–1000 keV fluences in  $\text{erg cm}^{-2} \text{s}^{-1}$  for the GRBs are color-coded. (b), (c) Polarization fractions of the GRBs are shown with  $\alpha$  (b) and  $\beta$  (c) obtained from Band function fits to the time-integrated burst spectra. The red circles represent GRBs with Bayes factor above 3 whereas the black down arrows represent the GRBs with Bayes factor less than 3.

In Figures 5(b) and (c), we also plot PF versus  $\alpha$  and  $\beta$  of the time-integrated burst spectra of our GRBs. No significant trend is observed between PF and the spectral slopes. Interestingly, we note that one GRB (180427A) exhibits a high polarization of 37%–83% while its time-integrated spectrum has a hard  $\alpha \sim -0.3$  and steep  $\beta \sim -2.8$ . The spectrum is suggestive of photospheric emission, in which case a high polarization can be observed only when viewed outside the jet opening angle (Waxman 2003; Chand et al. 2018). This case emphasizes that high PF alone cannot provide a full diagnostic of the emission mechanism, rather a spectropolarimetric study is required to get a better handle.

As discussed earlier, the PF could not be constrained for a majority of the bursts in our sample, indicating a low to null average polarization over the burst duration in these cases. This finding is consistent with that reported by POLAR for their sample of the study. The observed PF averaged over the burst can remain low to null due to either the radiation being intrinsically unpolarized or the angle of polarization varying temporally or with energy across the burst emission.

### 5.3. Improvements in the Polarization Analysis Techniques

Compared to the earlier work on GRB polarization using CZTI, we have made the following significant modifications in the analysis technique: (a) inclusion of low-gain pixels and thus an increase in the effective area and the energy range, (b) correction for two-pixel events generated by charge sharing, and (c) noise reduction. We find that the Compton noise reduction has a marginal impact on the results for most of the GRBs. In a few cases where the number of noisy events is large, the excess events arising from the pairs of noisy pixels might enhance counts in certain azimuthal bins and thereby can give an artificially higher amplitude of modulation.

The correction for charge sharing, on the other hand, is extremely important in removing systematic effects in the modulation curves. As mentioned earlier, the ratio of edge to corner pixel bins is lower in simulations if we do not consider charge sharing. In that case, even after geometric correction for completely unpolarized radiation, the modulation curve would still not be flat, with the edge bins and corner bins separated by a statistically significant amount. A sinusoidal fit to this modulation curve would yield a lower amplitude or

polarization fraction but in general with a high detection significance because the values in alternate bins are often outside the error bars of each other. We find that without correction for charge sharing, the estimated polarization fractions are lower but with slightly better detection significance. It is important to account for the effect of charge sharing in simulations to remove these systematics from the modulation curves.

The inclusion of the low-gain pixels increases the number of Compton events by 30%–40% and, more importantly, extends the energy range to 600 keV. We find that the background is higher at higher energies and hence the resultant improvement in the detection significance is marginal. The extension of the energy range, however, makes the results robust and will help us in possible future energy-resolved spectropolarimetry.











We have reanalyzed all the published polarization results based on CZTI data using the new method and find that the results are consistent with the published ones, albeit with reduced significance. The upper limits as derived with the new method are consistent with those published earlier. However, for GRB 160802A (Chattopadhyay et al. 2019) and GRB 160821A (Sharma et al. 2019), we see the detection significance in polarization fraction has been reduced in the new method. The apparent lower errors in the older method resulted from the absence of correction for charge sharing. For GRB 160821A, even with the new method, we find the  $\sim 90^\circ$  change in the polarization angle across the first and second parts and second and third parts of the prompt emission, albeit with reduced significance.

## 6. Conclusions

The polarization of GRB prompt emission is still an underexplored field among astronomical observations. It is highly challenging because the transient nature of GRBs results in poor photon statistics and also due to the involvement of nontrivial instrument systematics. The comprehensive analysis presented here for the five-year data from CZTI, in conjunction with the polarization results presented for a sample of GRBs using POLAR (Zhang et al. 2019; Kole et al. 2020), demonstrates that a large fraction of GRBs show low polarization. There exists, however, a significant fraction of GRBs ( $\sim 14\%$ – $25\%$ ) showing high hard X-ray polarization ( $\geq 40\%$ ). In these samples the number of detections so far is too low to attempt correlation studies with other observed properties of the prompt emission. On the other hand, the high polarization fraction in a few GRBs, with a hint of variability in the polarization fraction and polarization angle, offers an opportunity to study these variations and associate them with the other observables. We plan to undertake a systematic exploration of time-resolved spectropolarimetry of the GRBs with high polarization. CZTI is in its seventh year of operation and it continues to provide valuable information on GRB polarization. We plan to conduct detailed prompt and afterglow emission measurements of bright GRBs with a view to associating various observed properties with polarization variations. In future, dedicated polarimetric instruments such as LEAP (McConnell et al. 2021), POLAR-2 (Kole 2019), Daksha<sup>16</sup> (a multimessenger astronomical mission proposed to the Indian Space Research Organization), etc. will enable more such spectropolarimetric measurements.

This publication uses data from the AstroSat mission of the Indian Space Research Organization (ISRO), archived at the Indian Space Science Data Centre (ISSDC). CZTI Imager is built by a consortium of Institutes across India including Tata Institute of Fundamental Research, Mumbai, Vikram Sarabhai Space Centre, Thiruvananthapuram, ISRO Satellite Centre, Bengaluru, Inter University Centre for Astronomy and Astrophysics, Pune, Physical Research Laboratory, Ahmedabad, Space Application Centre, Ahmedabad: contributions from the vast technical team from all these institutes are gratefully acknowledged. D.F. acknowledges support from RSF grant 21-12-00250. This research has also made use of data obtained through the High Energy Astrophysics Science Archive Research Center Online Service, provided by the NASA/Goddard Space Flight Center.

## ORCID iDs

Tanmoy Chattopadhyay  <https://orcid.org/0000-0003-4905-7801>  
 Shabnam Iyyani  <https://orcid.org/0000-0003-3220-7543>  
 Vidushi Sharma  <https://orcid.org/0000-0002-4394-4138>  
 Anastasia Tsvetkova  <https://orcid.org/0000-0003-0292-6221>  
 N. P. S. Mithun  <https://orcid.org/0000-0003-3431-6110>  
 A. R. Rao  <https://orcid.org/0000-0003-0833-0533>  
 Santosh Vadawale  <https://orcid.org/0000-0002-2050-0913>  
 Varun Bhalerao  <https://orcid.org/0000-0002-6112-7609>  
 Dipankar Bhattacharya  <https://orcid.org/0000-0003-3352-3142>  
 Dmitry Frederiks  <https://orcid.org/0000-0002-1153-6340>

## References

- Abbott, B. P., Abbott, R., Abbott, T., et al. 2017, *ApJL*, 848, L13  
 Agostinelli, S., Allison, J., Amako, K., et al. 2003, *NIMPA*, 506, 250  
 Ahlgren, B., Larsson, J., Nymark, T., Ryde, F., & Pe'er, A. 2015, *MNRAS*, 454, L31  
 Ahlgren, B., Larsson, J., Valan, V., et al. 2019, *ApJ*, 880, 76  
 Band, D., Matteson, J., Ford, L., et al. 1993, *ApJ*, 413, 281  
 Burgess, J. M. 2014, *MNRAS*, 445, 2589  
 Burgess, J. M., Bégué, D., Greiner, J., et al. 2020, *NatAs*, 4, 174  
 Burgess, J. M., Kole, M., Berlato, F., et al. 2019, *A&A*, 627, A105  
 Chand, V., Chattopadhyay, T., Oganessian, G., et al. 2019, *ApJ*, 874, 70  
 Chand, V., Chattopadhyay, T., Iyyani, S., et al. 2018, *ApJ*, 862, 154  
 Chattopadhyay, T. 2021, *JApA*, 42, 106  
 Chattopadhyay, T., Vadawale, S. V., Rao, A. R., et al. 2016, *Proc. SPIE*, 9905, 99054D  
 Chattopadhyay, T., Vadawale, S. V., Rao, A. R., Sreekumar, S., & Bhattacharya, D. 2014, *ExA*, 37, 555  
 Chattopadhyay, T., Vadawale, S. V., Aarthy, E., et al. 2019, *ApJ*, 884, 123  
 Chattopadhyay, T., Gupta, S., Sharma, V., et al. 2021, *JApA*, 42, 82  
 Covino, S., & Gotz, D. 2016, *A&AT*, 29, 205  
 Duncan, R. C., & Thompson, C. 1992, *ApJL*, 392, L9  
 Eichler, D., Livio, M., Piran, T., & Schramm, D. N. 1989, *Natur*, 340, 126  
 Gill, R., Granot, J., & Kumar, P. 2020, *MNRAS*, 491, 3343  
 Gill, R., Kole, M., & Granot, J. 2021, *Galax*, 9, 82  
 Granot, J., & Königl, A. 2003, *ApJL*, 594, L83  
 Gruber, D., Goldstein, A., von Ahlefeld, V. W., et al. 2014, *ApJS*, 211, 12  
 Iwamoto, K., Mazzali, P. A., Nomoto, K., et al. 1998, *Natur*, 395, 672  
 Iyyani, S., Ryde, F., Ahlgren, B., et al. 2015, *MNRAS*, 450, 1651  
 Klebesadel, R. W., Strong, I. B., & Olson, R. A. 1973, *ApJL*, 182, L85  
 Kole, M. 2019, ICRC (Madison, WI), 36, 572  
 Kole, M., De Angelis, N., Berlato, F., et al. 2020, *A&A*, 644, A124  
 Kumar, P., & Zhang, B. 2015, *PhR*, 561, 1  
 Lundman, C., Pe'er, A., & Ryde, F. 2014, *MNRAS*, 440, 3292  
 Lundman, C., Vurm, I., & Beloborodov, A. M. 2018, *ApJ*, 856, 145  
 MacFadyen, A. I., & Woosley, S. E. 1999, *ApJ*, 524, 262  
 Mate, S., Chattopadhyay, T., Bhalerao, V., et al. 2021, *JApA*, 42, 93  
 McConnell, M. L. 2017, *NewAR*, 76, 1

<sup>16</sup> <https://www.star-iitb.in/research/daksha>

- McConnell, M. L., Baring, M., Bloser, P., et al. 2021, *Proc. SPIE*, **11821**, 11821OP
- Mészáros, P. 2006, *RPPh*, **69**, 2259
- Narayan, R., Paczynski, B., & Piran, T. 1992, *ApJL*, **395**, L83
- Narayan, R., Piran, T., & Kumar, P. 2001, *ApJ*, **557**, 949
- Odaka, H., Asai, M., Hagino, K., et al. 2018, *NIMPA*, **891**, 92
- Piran, T. 2004, *RvMP*, **76**, 1143
- Produit, N., Bao, T., Batsch, T., et al. 2018, *NIMPA*, **877**, 259
- Ratheesh, A., Rao, A. R., Mithun, N. P. S., et al. 2021, *JApA*, **42**, 37
- Rees, M. J., & Meszaros, P. 1992, *MNRAS*, **258**, 41
- Rees, M. J., & Meszaros, P. 1994, *ApJL*, **430**, L93
- Ryde, F. 2004, *ApJ*, **614**, 827
- Sari, R., Piran, T., & Narayan, R. 1998, *ApJL*, **497**, L17
- Scargle, J. D. 1998, *ApJ*, **504**, 405
- Scargle, J. D., Norris, J. P., Jackson, B., & Chiang, J. 2013, *ApJ*, **764**, 167
- Sharma, V., Iyyani, S., Bhattacharya, D., et al. 2020, *MNRAS*, **493**, 5218
- Sharma, V., Iyyani, S., Bhattacharya, D., et al. 2019, *ApJL*, **882**, L10
- Svinkin, D. S., Frederiks, D. D., Aptekar, R. L., et al. 2016, *ApJS*, **224**, 10
- Toma, K., Sakamoto, T., Zhang, B., et al. 2009, *ApJ*, **698**, 1042
- Tsvetkova, A., Frederiks, D., Golenetskii, S., et al. 2017, *ApJ*, **850**, 161
- Tsvetkova, A., Frederiks, D., Svinkin, D., et al. 2021, *ApJ*, **908**, 83
- Usov, V. V. 1992, *Natur*, **357**, 472
- Vadawale, S. V., Chattopadhyay, T., Rao, A. R., et al. 2015, *A&A*, **578**, 73
- Vadawale, S. V., Chattopadhyay, T., Mithun, N. P. S., et al. 2018, *NatAs*, **2**, 50
- Waxman, E. 2003, *Natur*, **423**, 388
- Woosley, S. E. 1993, *ApJ*, **405**, 273
- Yonetoku, D., Murakami, T., Gunji, S., et al. 2011a, *PASJ*, **63**, 625
- Yonetoku, D., Murakami, T., Gunji, S., et al. 2011b, *ApJL*, **743**, L30
- Yonetoku, D., Murakami, T., Gunji, S., et al. 2012, *ApJL*, **758**, L1
- Zhang, B.-B., Uhm, Z. L., Connaughton, V., Briggs, M. S., & Zhang, B. 2016, *ApJ*, **816**, 72
- Zhang, S.-N., Kole, M., Bao, T.-W., et al. 2019, *NatAs*, **3**, 258